Study of structural and photocatalytic activity of ZnO nanoparticles derived through ZIF-8 prepared at room-temperature

Himanshu[1], Aashish Sharma[1], Deepika[1], Aayush Gupta[2], Sachin Kumar[3], Gourav Singla[1*]

[1] Department of Physics, University Institute of Sciences, Chandigarh University, Mohali, Punjab

[2] Department of Mechanical Engineering, GLA University, Mathura 281406, India

[3]NanoScience Technology Center, University of Central Florida, Orlando, Florida 32826, United States

Abstract. In this study, we have prepared ZnO nanoparticles and investigated their structural as well as photocatalytic degradation of methylene blue (MB). Herein, we have explored the synthesis of ZnO nanoparticles at different calcination temperatures (500°C and 600°C) by using ZIF-8 as a precursor, which is prepared at room temperature. The resulting ZnO nanoparticles were characterized using techniques like X-ray diffraction (XRD), scanning electron microscopy (SEM) and UV-Visible spectroscopy to confirm their structural and optical properties. The photocatalytic activity of the prepared ZnO nanoparticles was evaluated by studying the degradation of organic pollutants under visible light irradiation. ZIF-8-derived ZnO nanoparticles obtained at 500°C displayed excellent photocatalytic activity as compared to another sample obtained at 600°C.

Keywords: ZnO nanoparticles; Williamson-Hall analysis; ZIF-8; Calcination.

1 Introduction

Over recent decades, several efforts have been made for the treatment of wastewater pollutants initiated by synthetic dyes, primarily employed in textile manufacturing. Due to the high solubility and stability of these synthetic dyes, several traditional methods like biological treatment, electrochemical treatment, oxidation, reduction, precipitation, and adsorption still give rise to undesirable drawbacks [1]. Therefore, photodegradation technology under the illumination of light is regarded as one of the alternative routes for the purification of water because of its significant performance for the degradation of toxic and nondegradable pollutants in wastewater without involving complex technologies [2]. Ever since it was found that TiO2 [3, 4] is the most widely used photocatalyst due to its suitable optical and electrical characteristics as well as well as contribute in the process of producing H2 from water. A variety of other sub-

S. Kumar et al. (eds.), *Proceedings of the 2nd International Conference on Advanced Materials & Devices for Futuristic Applications-2024 (IC-AMDFA 2024)*, Atlantis Highlights in Materials Science and Technology 5,
https://doi.org/10.2991/978-94-6239-695-1_15

stances have also been used in photocatalytic processes, such as metal sulfides, oxides, MOFs, and g-C3N4 [5-10]. Among them, the metal oxide-based semiconductor material zinc oxide (ZnO) with a band gap of 3.2 eV has received a lot of attention as a photocatalyst because of its high photo reactivity, great photostability, non-toxicity, low cost, strong oxidation capability and chemical stability [11]. It is capable of degrading organic dyes into non-toxic compounds. With the advancement in science and technology, improvements in the photocatalytic behavior of ZnO are required by making modifications in the preparation of ZnO nanoparticles.

In recent years, the field of functional materials has witnessed remarkable advancements, driven by the exploration of innovative synthesis strategies and the discovery of novel precursor materials [12]. Among these, zeolitic imidazolate frameworks (ZIF) have emerged as a particularly intriguing class of materials due to their unique structural characteristics, including tunable porosity, high surface area, and versatile chemical compositions [13]. Within this context, the synthesis of metal oxide materials from ZIF has garnered considerable attention, fueled by the promise of tailoring the properties of the resulting oxides for a wide range of applications, from catalysis to energy storage [14].

The pursuit of a simple, time-efficient, and energy-saving method for synthesizing ZnO continues to draw significant scientific interest. In this study, we present a straightforward approach to synthesize ZnO nanoparticles by calcining ZIF-8 precursors, prepared at room temperature, at two different temperatures. We then investigate the structural, optical, and photocatalytic properties of the resulting ZnO nanoparticles, using a modified Williamson–Hall (W–H) analysis and evaluating their performance in methylene blue (MB) degradation with different thermal treatment temperature.

2 Experimental

2.1 Chemicals

Zinc nitrate hexahydrate [$Zn(NO_3)_2.6H_2O$, >98%], 2-Methylimidazole [$CH_3C_3H_2N_2H$, >98%], methanol [CH_3OH, >98%] were purchased from Loba Chemie Pvt. Lmt. All chemicals were used directly without any further purification.

2.2 Synthesis of ZnO nanoparticles

Dissolve the zinc precursor and imidazole linker in 50ml methanol. The specific concentrations will depend on the desired ZIF structure and final ZnO properties. Stir the solution thoroughly using a magnetic stirrer for 30 minutes to ensure complete mixing of the precursors. Apply sonication for a predetermined period to promote faster nucleation and crystal growth of ZIF nanoparticles. Allow the reaction mixture to rest for 24 hours. The ZIF crystals will precipitate out of the solution. Wash the precipitate with fresh methanol to remove residual solvent and impurities. Dry the collected white powder at room temperature using a low-temperature oven (around 60°C) to remove any remaining solvent. The dried ZIF powder was placed in alumina

crucible and subject to heat treatment in air at a controlled temperature of 500°C and 600°C for 2 hours. This process decomposes the organic framework of ZIF, leaving behind porous ZnO nanoparticles (ZnO-NPs). The structural investigation of the prepared samples was done using X-ray diffraction by Rigaku diffractometer with Cu-Kα (λ = 1.54 Å) radiation source. Furthermore, the surface morphology of the sample was investigated by scanning electron microscopy carried out by the JSM-6400 microscope. The optical properties were examined by recording UV–Vis diffuse reflectance spectra (190–800 nm) using a Shimadzu UV-2600 spectrophotometer.

3 Results and discussion

3.1 XRD analysis

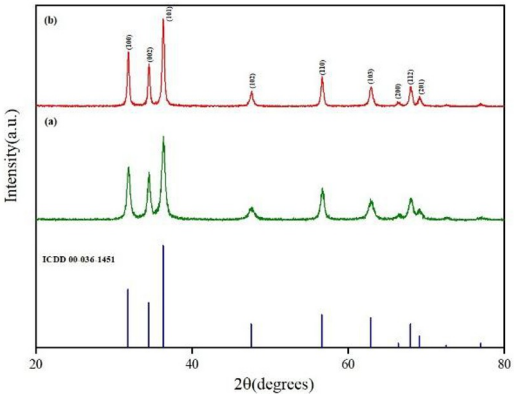

Figure 1. XRD graphs of ZnO nanoparticles obtained at **(a)** 500°C and **(b)** 600°C.

The X-ray diffraction (XRD) patterns for the ZnO samples obtained at separate temperature, 500°C (A500) and 600°C (A600), are shown in figure1. The entire set of XRD peaks corresponds to each plane closely matches with the standard reference pattern (ICDD 36-1451) [15], which reports to hexagonal structure with lattice constant (a=3.2498 Å, c= 5.2066 Å). Notably, both samples obtained at 500°C and 600°C exhibit their most intense peak, corresponding to the (101) crystallographic plane. It is evident that the reflection peaks become more distinct as the calcination temperature increases to 600°C, indicating an improvement in crystallinity. The lattice parameters, including the values of lattice constants (a and c) and unit cell volumes, are calculated using the lattice geometry equation [16-19]. The slight increase in lattice constant and volume clearly attributes the thermal effect on the crystallographic properties of prepared zinc-oxide nanoparticles.

Table 1: The crystallographic parameters of ZnO-NPs treated at 500°C and 600°C.

Tempera-ture	2 theta	hkl	Structure	Lattice parame-ter (nm)	V $(nm)^3$
500°C	31.8457	(100)	hexagonal	a=0.3241	0.051068
	34.46298	(002)	hexagonal	c/a = 1.6040	-
600°C	31.81692	(100)	hexagonal	a=0.3243	0.051198
	34.46341	(002)	hexagonal	c/a = 1.6025	-

3.2 Particle size and strain

3.2.1. Scherrer method

The diffraction peak widening due to the microstrain and dislocation-related lattice defects can also be assessed by the XRD analysis. The size of prepared oxide nanoparticles was evaluated through X-ray line broadening after applying the Scherrer equation:

$$D = \left(\frac{k\lambda}{\beta_{hkl} cos\theta_{hkl}}\right) \quad (1)$$

where θ_{hkl} is the peak location, β_{hkl} is the peak breadth at half-maximum intensity, k is a constant equal to (0.9), λ is the wavelength of the radiation (1.5406 Å) and D is the particle size in nanometers.

3.2.2. Williamson-Hall methods

The Williamson-Hall plot was generated using XRD data to examine peak broadening by the following equation.

$$\beta_{hkl} Cos\theta_{hkl} = \left(\frac{k\lambda}{D}\right) + (4\varepsilon sin\theta_{hkl}) \quad (2)$$

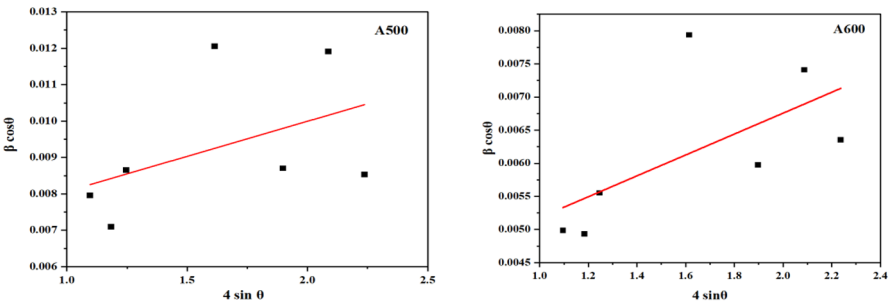

Figure 2. UDM graph for the ZnO sample obtained at **(a)** 500°C and **(b)** 600°C.

The parameters of the fitted linear line (slope and intercept) were extracted from the plot between $\beta_{hkl}\cos\theta_{hkl}$ and $4\sin\theta_{hkl}$ shown in figure 2 for both samples A500 and A600 represent the strain and particle size, respectively. Furthermore, the equation (2) represents the model known as Uniform Deformation Model (UDM). In UDM, it was considered that the crystal's structure is isotropic in nature and the strain was assumed to be uniform in all directions within the crystal [20].

3.2.4. Uniform Stress Deformation Model (USDM)

The current model described Hooke's law a relation between stress and strain represented by $\sigma=Y\epsilon$, where σ is the stress inside the crystal and Y is its modulus of elasticity [20]. This equation is useful to calculate only for a very micro strain. Hooke's law can be applied in this case by assuming that the ZnO-NPs include a tiny strain.

$$\beta_{hkl}cos\theta = \left(\frac{k\lambda}{D}\right) + \left(\frac{4\sigma sin\theta_{hkl}}{Y_{hkl}}\right) \quad (3)$$

For a hexagonal crystal system, the Young's modulus is given by the following relation [21]

$$Y_{hkl} = \frac{\left[\frac{(h^2+(h+2k)^2)}{3} + \left(\frac{al}{c}\right)^2\right]}{S_{11}(h^2+(h+2k)^2)^2 + S_{33}\left(\frac{al}{c}\right)^4 + (2S_{13}+S_{44})\left(h^2+\frac{(h+2k)^2}{3}\right)\left(\frac{al}{c}\right)^2}$$

Where s_{11}, s_{13}, s_{33} and s_{44} correspond to the elastic compliances of zinc oxide (ZnO) having specific values [22]. The analysis revealed that the prepared zin oxide nanoparticles have a Young's modulus of approximately 127 GPa. The plots between $(4\sin\theta)/Y_{hkl}$ and $\beta_{hkl}\cos\theta$ for both samples A500 and A600, were used to determine stress from the slope of the fitted line.

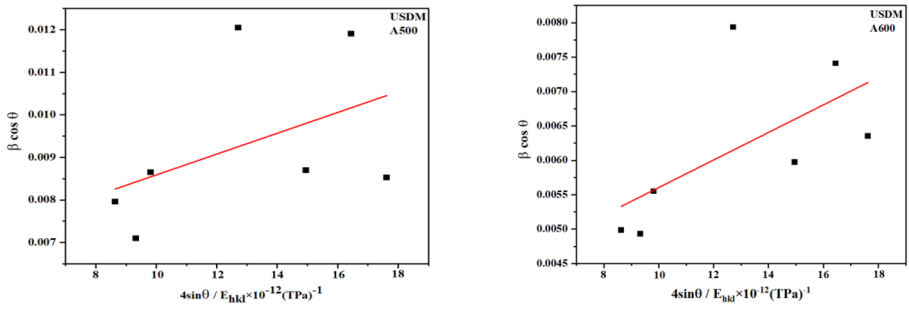

Figure 3. USDM for ZnO sample obtained at **(a)** 500°C and **(b)** 600°C.

3.2.5. Uniform deformation energy density model (UDEDM)

The UDEDM, a different variation of the Williamson-Hall methods, is employed to determine the energy density (u_{ed}) of the crystal. For elastic systems that adhere to Hooke's law, the relationship between strain and □□□ is expressed as ($\epsilon^2 \times Y_{hkl}$)/2 [23]

$$\beta_{hkl} cos\theta_{hkl} = \left(\frac{k\lambda}{D}\right) + \left(4 sin\theta_{hkl} \left(\frac{2u_{ed}}{Y_{hkl}}\right)^{0.5}\right) \quad (4)$$

After plotting $\beta_{hkl}Cos\theta_{hkl}$ versus $4sin\theta \left(\frac{2u_{ed}}{Y_{hkl}}\right)^{0.5}$, we can calculate the anisotropic energy density (□□□) using the slope, the crystallite size (D) is approximated from the intercept. While the stress (□) and microstrain (□) are computed from (□□□) and Y_{hkl} [23]. Figure 4 shows the UDEDM for each of the samples, and Table 2 lists the outcomes.

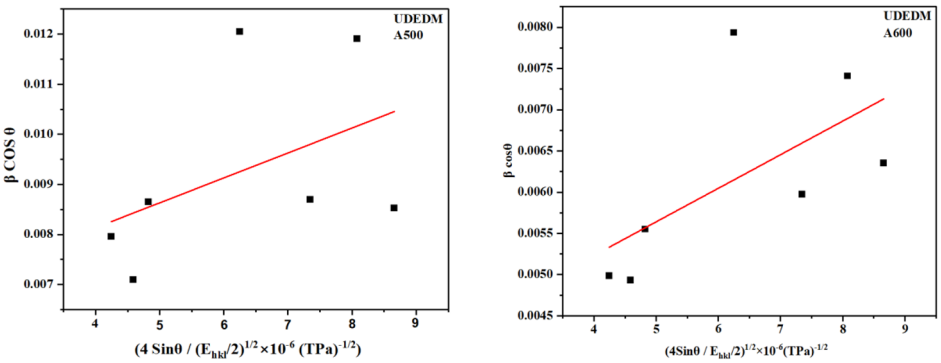

Figure 4. UDEDM for the ZnO sample obtained at **(a)** 500°C and **(b)** 600°C.

Applying the UDM, UDSM, and UDEDM models yields nearly equal mean crystallite size values, indicating that the introduction of strain to the modified W–H equations does not alter the average value of crystallite size. Even though all Williamson-Hall models for the sample annealed at 600°C show incredibly large crystallite sizes, according to previously published data [24], all of the ε and σ values found using all of the Williamson-Hall models decrease inversely with the crystallite size [25, 26]. When comparing the information produced by the three models, it is evident that there is a lot of similarity in the parameter values that verify the nanoparticle's isotropic nature.

Table 2. Ordered parameters of ZnO-NPs obtained at 500°C and 600°C.

Temperature	Scherrer method	Williamson-Hall method								
		UDM		USDM			UDEDM			
	D(nm)	D (nm)	ε no unit × 10^{-3}	D(nm)	ε no unit × 10^{-3}	σ (MPa)	D (nm)	ε no unit × 10^{-3}	σ (MPa)	u (KJm^{-3})
500°C	18	23	1.93	23	1.92	244	23	1.97	250	247
600°C	27	39	1.58	39	1.57	200	39	1.61	204	165

3.3 Scanning Electron Microscopy (SEM)

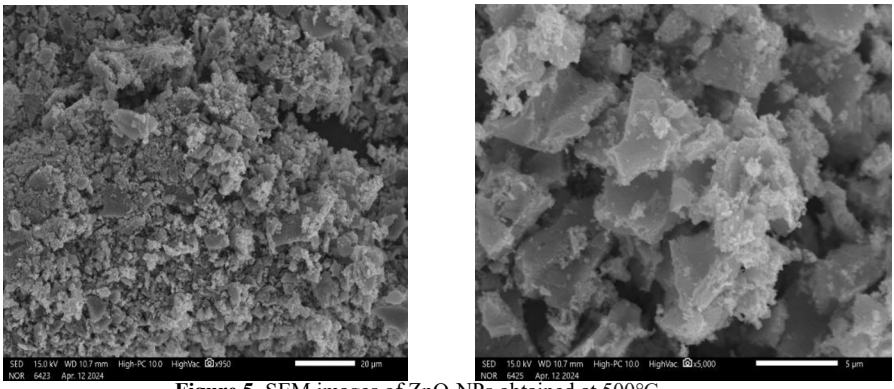

Figure 5. SEM images of ZnO NPs obtained at 500°C.

SEM imaging (Figure 5) revealed distinctive morphological features of the ZIF-derived ZnO sample. The micrographs exhibit homogeneous distribution with faceted morphology of the ZnO nanoparticles sticking together after calcination. Additionally, the ZnO-NPs are encapsulated in porous carbon, which contributes to enhanced photocatalytic activity.

3.4 UV-visible spectroscopy

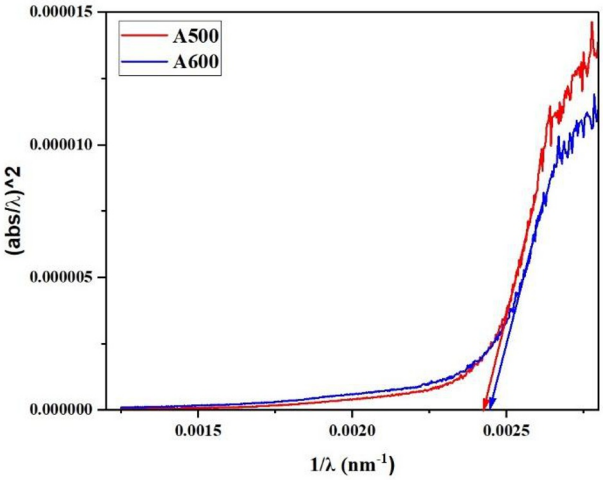

Figure 6. UV-vis spectra of ZnO nanoparticles obtained at 500°C and 600°C.

Figure 6 shows the UV-vis optical spectra of ZnO nanoparticles obtained after the thermally decomposition of ZIF-8 at 500 °C and 600 °C. The spectra were used to investigate the modification in the band gap of ZnO nanoparticles with temperature. The value of band gap (E_{gap}), can be estimated using $E_{gap}=1239.83/\lambda_g$. The value of λ_g will be evaluated by extrapolating the linear of the $(Abs(\lambda)/\lambda)^{1/m}$ vs. $1/\lambda$ for m=1/2 [27].

Figure 6 clearly illustrates the influence of temperature on the optical band gap. As the temperature increases, the optical band gap widens—from 2.90 eV for sample A500 to 2.94 eV for sample A600. This increase is attributed to the reduction of localized defect states within the band gap, leading to an overall enhancement in band gap energy

3.5 Photocatalytic activity

The degradation of methylene blue (MB) is used to assess the photocatalytic behavior of the obtained samples. The adsorption-desorption equilibrium was established in the dark reactor for 6 hours prior to recording the dye removal as a result of photoexcitation of the produced catalysts. The elimination of MB dye under visible (100W white LED) irradiation is then depicted in figure 7, employing a 20 mg/L catalyst in 100 ml of dye solution.

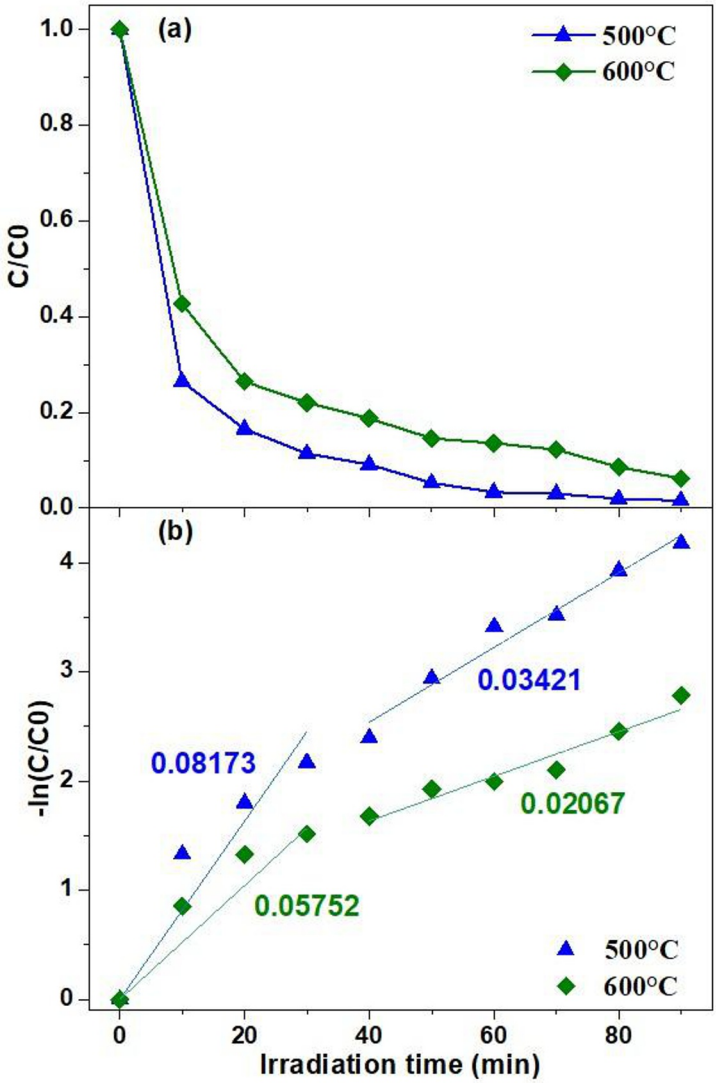

Figure 7. (a) Relative removal, and (b) pseudo first order kinetics of MB dye under visible LED irradiation by using ZnO-NPs obtained at 500°C and 600°C.

As seen in figure 7(a), an aliquot was taken from the reaction media at 10-minute intervals to document the temporary dye elimination. It was found that at the calcination temperature of 500°C, the overall elimination of MB dye is observed to be 98.05%. On the other hand, catalytic performance was reduced (93.16%) by doing calcination at 600°C. Physisorption was taken into consideration for the successful contact between dye molecules and the catalyst surface in order to comprehend the kinetics of photochemical reactions using the pseudo first order rule. A rapid interac-

tion was seen during the first 30 minutes of the two-step adsorption process shown in figure7(b), but after that time, the photochemical reaction slowed down. Figure 7(b) lists all of the rate constants (min^{-1}) and shows that, when compared to other calcined ZnO powders, the ZnO catalyst calcined at 500°C had the greatest rate constant. Similar outcomes involving the multistep degradation of rhodamine B dye, have previously been reported by Kaur et al. [28]

4. Conclusions

This work reported a successful synthesis of ZnO nanoparticles derived through ZIF-8 prepared at room-temperature. The structure and morphology of the samples were characterized using XRD and SEM. The XRD results indicate that the prepared ZnO nanoparticles are well-crystalline in nature. Further, XRD analysis is also used to calculate strain, stress and energy density by following different methods, such as the modified Scherrer, W–H plot, via XRD peak broadening analysis. From the SEM results, we have observed a facetated morphology of ZnO nanoparticles of uniform size, indicating effective production and control over the distribution of particle sizes. From the analysis of the UV-Vis absorption spectra, we have observed a variation in the band gap of the obtained ZnO nanoparticles with temperature. The assessment of photocatalytic activity demonstrated the effective breakdown of MB dye when exposed to white light, underscoring the superior photocatalytic capabilities of the ZnO nanoparticles that were produced after calcination of ZIF-8 at 500°C.

Acknowledgements

The authors are thankful to Chandigarh University for providing financial support to carry out this work. One of the authors (AG) thanks to Department of Science and Technology, India (SERB) for providing financial assistance to carry out this research work under Start-up Research Grant (SRG/2022/000630 dated 03.11.2022).

References

1. Adeel, M., Saeed, M., Khan, I., Muneer, M., Akram, N.: Synthesis and Characterization of Co–ZnO and Evaluation of Its Photocatalytic Activity for Photodegradation of Methyl Orange. ACS Omega **6,** 1426-1435 (2021).
2. Chen, R. X., Zhu, S. L., Mao, J., Cui, Z. D., Yang, X. J., Liang, Y. Q., Li, Z. Y.: Synthesis of CuO/Co3O4 Coaxial Heterostructures for Efficient and Recycling Photodegradation. International Journal of Photoenergy. **2015,** 183468 (2015).
3. Yang, X. B., Huang, L. Q., Du, G. Q., Lu, X. T.: ZIF-8 derived Ag-doped ZnO photocatalyst with enhanced photocatalytic activity. Journal of Porous Materials. **24**, 881-886 (2017).
4. Low, J. X., Cheng, B., Yu, J. G.: Surface modification and enhanced photocatalytic CO_2 reduction performance of TiO_2: a review. Applied Surface Science. **392**, 658-686 (2017).
5. Zhan, W., Sun, L., Han, X.: Recent progress on engineering highly efficient porous semiconductor photocatalysts derived from metal–organic frameworks. Nano-Micro Letters **11,** 1 (2019).

6. Huo, Q., Zhao, J., Li, J., Wang, B., Liu, S.: ZnO-rich CdS-ZIF-8 catalyst for enhanced visible-light photocatalytic degradation of methylene blue. Research on Chemical Intermediates. **44**, 2347-2364 (2017).
7. Sun, L., Li, R., Zhan, W., Yuan, Y., Wang, X., Han, X., Zhao, Y.: Double-shelled hollow rods assembled from nitrogen/sulfur-codoped carbon coated indium oxide nanoparticles as excellent photocatalysts. Nature Communications. **10**, 2270 (2019).
8. Qi, K., Cheng, B., Yu, J., Ho, W.: Review on the improvement of the photocatalytic and antibacterial activities of ZnO. Journal of Alloys and Compounds. **727**, 792-820 (2017).
9. Thanh, M. T., Thien, T.V., Du, P.D., Hung, N.P., Khieu, D.Q.: Iron doped zeolitic imidazolate framework (Fe-ZIF-8): synthesis and photocatalytic degradation of RDB dye in Fe-ZIF-8. Journal of Porous Materials. **25**, 857-869 (2017).
10. Zhao, X., Yang, H., Jing, P., Shi, W., Yang, G., Cheng, P.: A Metal-Organic Framework Approach toward Highly Nitrogen-Doped Graphitic Carbon as a Metal-Free Photocatalyst for Hydrogen Evolution. Small **13,** 1603279 (2017).
11. Ahmad, I., Akhtar, M. S., Ahmed, E., Ahmad, M., Keller, V., Khan, W. Q., Khalid, N.R.: Rare earth co-doped ZnO photocatalysts: Solution combustion synthesis and environmental applications. Separation and Purification Technology **237**, 116328 (2020).
12. Jun, J. H., Seong, H., Cho, K., Moon, B.-M., Kim, S.: Ultraviolet photodetectors based on ZnO nanoparticles. Ceramics International **35,** 2797-2801 (2009).
13. Torad, N. L., Hu, M., Ishihara, S., Sukegawa, H., Belik, A. A., Imura, M., Ariga, K., Sakka, Y., Yamauchi, Y.: Direct Synthesis of MOF-Derived Nanoporous Carbon with Magnetic Co Nanoparticles toward Efficient Water Treatment. Small **10**, 2096-2107 (2014).
14. Pan, Y., Liu, Y., Zeng, G., Zhao, L., Lai, Z.: Rapid synthesis of zeolitic imidazolate framework-8 (ZIF-8) nanocrystals in an aqueous system. Chemical Communications. **47**, 2071-2073 (2011).
15. Shah, A. P., Jain, S., Mokale, V. J., Shimpi, N. G.: High performance visible light photocatalysis of electrospun PAN/ZnO hybrid nanofibers. Journal of Industrial and Engineering Chemistry. **77**, 154-163 (2019).
16. Seetawan, U., Jugsujinda, S., Seetawan, T., Ratchasin, A., Euvananont, C., Junin, C., Thanachayanont, C., Chainaronk, P.: Effect of Calcinations Temperature on Crystallography and Nanoparticles in ZnO Disk. Materials Sciences and Applications **2**, 1302-1306 (2011).
17. Pandiyarajan, T., Karthikeyan, B.: Cr doping induced structural, phonon and excitonic properties of ZnO nanoparticles. Journal of Nanoparticle Research **14**, 647 (2012).
18. Pal, U., Serrano, J. Garcia, Santiago, P., Xiong, G., Ucer, K.B., Williams, R.T.: Synthesis and optical properties of ZnO nanostructures with different morphologies. Optical Materials **29**, 65-69 (2006).
19. Cullity, B. D. : Elements of X-Ray Diffraction, Addison-Wesley Publishing Company Inc. 531 (1956).
20. Zak, A. K., Majid, W. A., Abrishami, M. E., Yousefi, R.: X-ray analysis of ZnO nanoparticles by Williamson-Hall and size-strain plot methods. Solid State Sciences **13**, 251-256 (2011).
21. Zhang, J., Zhang, Y., Xu, K.W., Ji, V.: General compliance transformation relation and applications for anisotropic hexagonal metals. Solid State Communications. **139**, 87-91 (2006).
22. Nye, J. F.: Oxford, Physical Properties of Crystals, Clarendon Press, Oxford (1985).
23. Ismail, M. A., Taha, K. K., Modwi, A., Khezami, L.: ZnO Nanoparticles: Surface and X-Ray Profile Analysis. Journal of Ovonic Research **14**, 381-393 (2018).

24. Mote, V., Purushotham, Y., Dole, B.: Williamson-Hall analysis in estimation of lattice strain in nanometer-sized ZnO particles. Journal of Theoretical and Applied Physics **6**, 6 (2012).
25. Jacob, R., Isac, J.: X-ray diffraction line profile analysis of $Ba_{0.6}Sr_{0.4}Fe_xTi_{(1-x)}O_3$ (x=0.4). International Journal of Chemical Studies **2**, 12-21 (2015).
26. Amirkhanlou, S., Ketabchi, M., Parvin, N.: Nanocrystalline/nanoparticle ZnO synthesized by high energy ball milling process. Materials Letters **86**, 122-124 (2012).
27. Ghobadi, N.: Band gap determination using absorption spectrum fitting procedure. International Nano Letters **3**, 1-4 (2013).
28. Kaur, G., Gupta, A., Wolski, L., Pandey, O. P.: CeO_2 supported $Zn_{1-x}Mn_xS$ (x: 0.025, 0.05, 0.075 and 0.10) catalyst for photoremoval of rhodamine B dye. Solar Energy **225**, 773-783 (2021).